Materials Characterization 174 (2021) 111025

Contents lists available at ScienceDirect

Materials Characterization

journal homepage: www.elsevier.com/locate/matchar

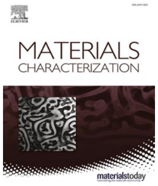

How microstructure affects localized corrosion resistance of stir zone of the AA2198-T8 alloy after friction stir welding

Caruline de Souza Carvalho Machado [a,*], Uyime Donatus [a], Mariana Xavier Milagre [a], João Victor de S. Araujo [a], Barbara Victoria G. de Viveiros [a], Rafael Emil Klumpp [a], Victor Ferrinho Pereira [b], Isolda Costa [a]

[a] Instituto de Pesquisas Energéticas e Nucleares (IPEN/CNEN), Av. Prof. Lineu Prestes, 2242, São Paulo, SP 05508-000, Brazil
[b] Brazilian Nanotechnology National Laboratory (CNPEM), R. Giuseppe Máximo Scolfaro 10000, Campinas, SP 13083-970, Brazil

ARTICLE INFO

Keywords:
Aluminum alloys
Localized corrosion
Friction stir welding
Electrochemical techniques

ABSTRACT

In this study, the microstructure and corrosion resistance of the stir zone (SZ) of the AA2198-T8 Al-Cu-Li alloy welded by friction stir welding (FSW) were investigated by microscopy, immersion tests and electrochemical techniques such as measurements of open circuit potential variation with time, and scanning vibrating electrode technique (SVET) measurements. A low chloride-containing solution (0.005 mol L^{-1} NaCl) was employed in the corrosion studies and severe localized corrosion (SLC) was observed in the SZ related to intergranular attack. The results were compared to those of the non-affected areas by FSW, also known as base metal (BM). In the BM, SLC was found and the type of attack related to it was intragranular. In both zones, BM and SZ, SLC was due to precipitates of high electrochemical activity, specifically T1 (Al_2CuLi) phase in the BM, whereas TB (Al_7Cu_4Li) / T2 (Al_6CuLi_3) in the SZ. Scanning vibrating electrode technique (SVET) analysis was very useful in the study of SLC in the AA2198-T8 alloy showing the development of high anodic current densities at the mouth of the SLC sites.

1. Introduction

Aluminum-lithium (Al—Li) alloys are known by their low density, which is related to the addition of Li as an alloying element. Besides the weight reduction, the presence of this element also improves the elastic modulus of Al alloys (for each 1 wt% of Li added, the elastic modulus increases by approximately 6% [1–3]). These characteristics showcase these materials as potential replacements for the conventional 2XXX series alloys used in the aeronautic sector. The AA2198 belongs to the third generation Al-Cu-Li alloys and has been developed to be used in applications where damage tolerance is a critical factor [2,4,5]. Although this alloy has already been employed in the aerospace industry [6], it is susceptible to localized corrosion [7–13]. Consequently, the corrosion resistance of Li-containing Al alloys has been extensively studied [14–22].

In the new generation Al-Cu-Li alloys, two major forms of localized corrosion have been observed. They differ from each other by the magnitude (or penetration) of the attack and are classified as non-severe localized corrosion (LC) and severe localized corrosion (SLC) [14,23]. In the LC, the attack is related to the micro-galvanic cell between the micrometric particles and matrix [24]. If the particles are cathodic to the matrix, the attack occurs in the surrounding matrix, resulting in trenching and shallow cavities [25]. In the SLC, the attack is usually associated with the active T1 phase (Al_2CuLi). Due to the potential difference between the T1 and the matrix, in the order of 0.2 V, strong galvanic coupling might occur [12,20]. Consequently, the distribution of T1 phase in the microstructure has an important role, leading to the preferential attack of grains containing a high density of this phase [11,12,26–29]. Two types of morphology related to SLC have already been reported in the literature: intragranular and intergranular. In both cases, SLC presents particular features, such as rings of corrosion products and cathodically protected areas surrounding the SLC, besides hydrogen gas evolution at the mouths of the pits [11,14,21].

High strength 2XXX series alloys are especially susceptible to weld cracking, which makes it difficult to employ conventional fusion welding techniques for their joints. In this sense, friction stir welding (FSW) is an alternative method of joining, since it is a solid-state welding process, which eliminates typical alloy melting defects [30,31]. The thermal and

---

[*] Corresponding author.
E-mail address: carulinemachado@yahoo.com.br (C. de Souza Carvalho Machado).

https://doi.org/10.1016/j.matchar.2021.111025
Received 16 September 2020; Received in revised form 28 February 2021; Accepted 1 March 2021

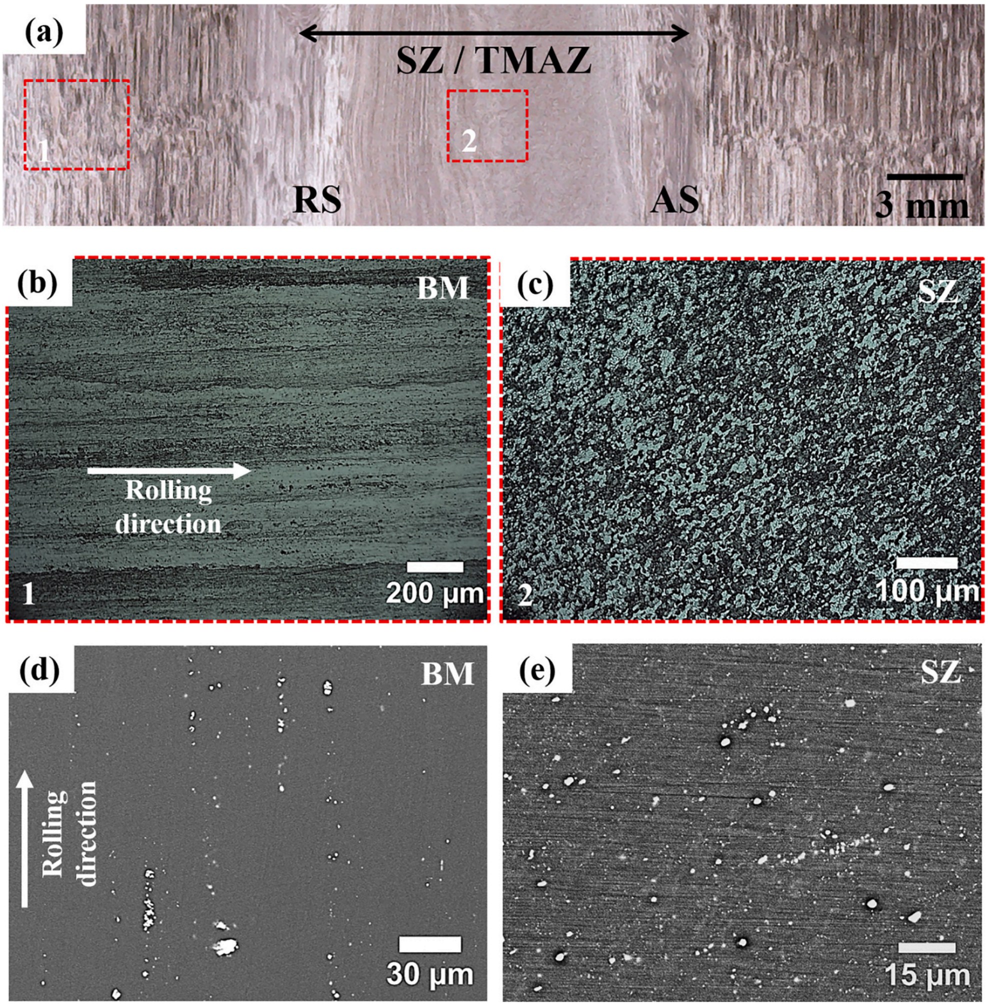

Fig. 1. (a) Optical macrograph of the 2198-T8 Al-Cu-Li alloy welded by FSW. (b,c) optical micrographs of the (b) base metal (BM) and (c) stir zone (SZ) corresponding to higher magnification of the dashed squares showed in figure (a), showing differences in grain morphologies. (d,e) Scanning electron micrographs of the (d) base metal (BM) and (e) stir zone (SZ) showing differences in size and distribution of constituent particles.

mechanical effects of FSW produce zones of different microstructures, such as the heat-affected zone (HAZ), the thermomechanically affected zone (TMAZ) and the stir zone (SZ). Also, part of the alloy remains unaffected by the welding process, and this is usually called the base metal (BM). In addition to the microstructural modification, all the zones affected by welding will present changes in the original mechanical and corrosion properties of the alloy. This can be especially relevant for the SZ due to its proximity to the tool, where a high level of deformation and temperature are achieved [31–36]. In this sense, several types of research have been focused on correlating the microstructure of the SZ with the variation of its thermal history and also to characterize its corrosion behavior [34,37–40]. It is expected that the SZ presents great differences in electrochemical behavior compared to the BM.

Corrosion resistance is an important issue in welded components since corroded areas can act as initiation sites for cracks, resulting in structural failures. In an attempt to prevent corrosion in welded components, several authors studied the corrosion resistance of welds to predict the most susceptible zones and explain their behavior [7,8,36,41]. In most studies, electrolytes composed of chlorides are employed, since they are ever-present in the environment and tend to attack the passive film of Al alloys. Frequently, solutions with a high concentration of chlorides have been used in electrochemical analyses to compare the performance of the different zones of weldments [7,8,38,41,42], leading to high kinetics of corrosion attack that generates large amounts of corrosion products. These products mask some of the phenomena involved, mainly those related to the interactions between the matrix, precipitates and the remaining passive layer. Therefore, a solution of low concentration is interesting to investigate the development of an attack. Also, this kind of solution is proper for use in SVET because they maximize the potential difference in the electrolyte [43].

In this study, it was found important to use a solution of low chloride concentration, that is, low corrosiveness (0.005 mol L^{-1} NaCl solution) in order to monitor the evolution of corrosion and contribute to the understanding of corrosion mechanisms of the SZ of the AA2198-T8 Al-Cu-Li alloy welded by FSW. This zone was chosen because it presents the foremost microstructural modification, compared to the parent material. Also, it allows for the evaluation of its behavior if it is exposed to the corrosive environment in isolation, such as when there is damage to the protection system in service. A comparison of the results with those of the BM was also carried out in order to understand how the microstructure affects the localized corrosion of the SZ after FSW.

2. Material and methods

2.1. Material

4 mm thick plates of the AA2198-T8 (3.32 wt% Cu, 0.96 wt% Li, 0.31 wt% Mg, 0.26 wt% Ag, 0.51 wt% Zr, 0.05 wt% Fe, 0.04 wt% Si,

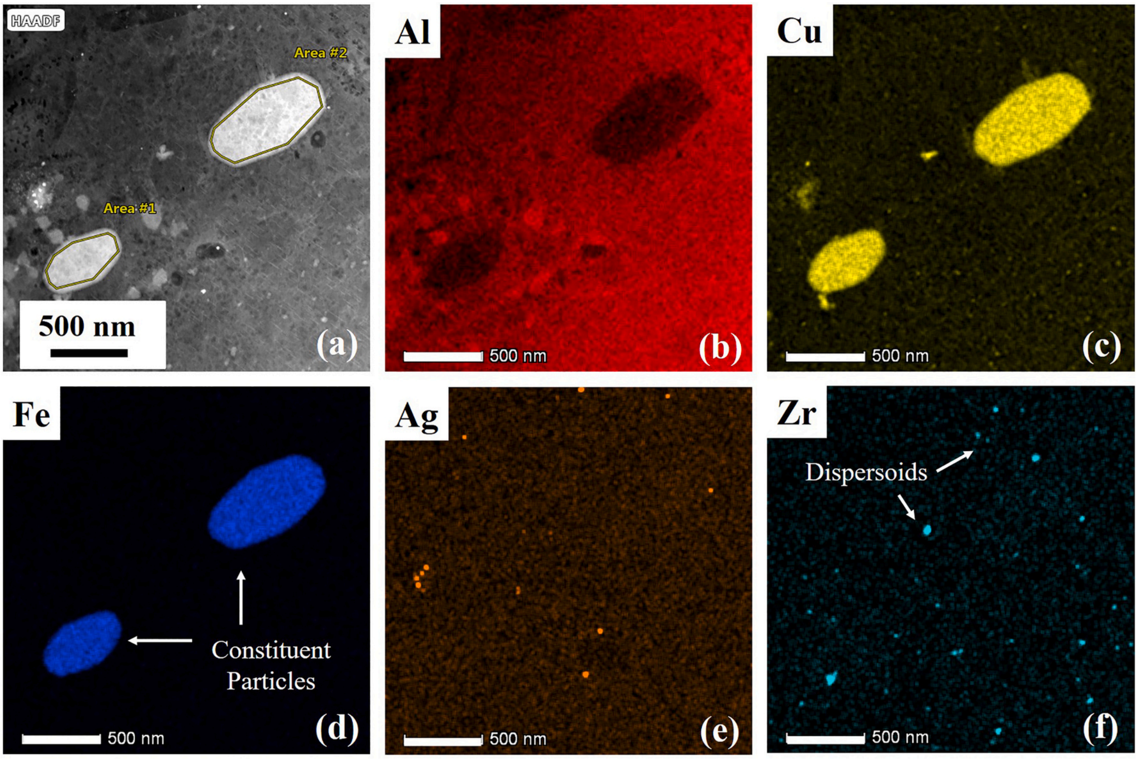

Fig. 2. (a) High angle annular dark field image of the base metal (BM); (b-f) EDX maps showing the distribution of (b) Al, (c) Cu, (d) Fe, (e) Ag and (f) Zr.

0.04 wt% Zn, 0.02 Mn) were used in this study. This alloy was recently characterized in [44]. Friction stir welding (FSW) was carried out in Brazilian Nanotechnology National Laboratory (LNNano) using a H13 tool steel with a 16 mm shoulder diameter and an adjustable pin of 3.75 mm in length. A rotation speed of 700 RPM and a transverse speed of 300 mm/min was used for the welding. Samples from the SZ and the BM were studied by evaluating their microstructure and corrosion resistance.

2.2. *Microstructural characterization*

The surface of the AA2198-T8 welded sample was prepared by conventional metallography (up to 1 μm surface finish) and then etched with a solution composed of 2 mL HF, 25 mL HNO_3 in 100 mL of distilled water for 10 s. Subsequently, the microstructure was observed by optical microscopy (Leica DMLM). In addition, images of the stir zone (SZ) and base metal (BM) were obtained using TM3000 scanning electron microscope (SEM). Specimens for transmission electron microscopy (TEM) were obtained by cutting 3 mm diameter discs from the SZ and BM. The samples were mechanically thinned and prepared by twin-jet electropolishing with a solution containing 20 (*v*/v) % HNO_3 in methanol at 25 V and − 30 °C. High angle annular dark-field (HAADF) and bright-field (BF) images were obtained in a JEOL 2100F microscope.

Samples from the SZ and the BM were ground with silicon carbide paper (up to #4000) before to perform differential scanning calorimetry (DSC) experiment equipment coupled to a TA-60WS. The data were obtained under nitrogen (99.999 wt%) atmosphere using a DSC-50 SHIMADZU equipment. The heating rate used in DSC measurements was 10 °C min^{-1} and the scanning temperature ranged from 50 to 550 °C.

2.3. *Corrosion evaluation*

Open circuit potential (OCP) was monitored with time of exposure to the 0.005 mol L^{-1} NaCl solution using an Ag/AgCl (KCl saturated) as a reference electrode. OCP was monitored for 8 h, after which the exposed surface was examined by optical microscopy and scanning electron microscopy (SEM). The SZ and BM were tested in isolation from the surrounding zones (using beeswax) to evaluate the effect of FSW on their electrochemical behavior without galvanic coupling effects. The area exposed to the test solution was 0.28 cm^2. All the measurements were performed after grinding and polishing the samples to a 1 μm diamond suspension finishing. Scanning vibrating electrode technique (SVET) tests were carried out using an Applicable Electronics™ SVET machine that is controlled by an Automated Scanning Electrode Technique (ASET 4.0) software. Insulated Pt—Ir probe was used as the vibrating electrode for the SVET system. A 15 μm diameter platinum sphere was electrodeposited at the tip of the probe. Prior to SVET tests, the machine was calibrated using a current source connected to a calibration electrode at a distance of 150 μm. A current value of 60 nA was used for calibration. The conductivity of the solution used was inputted into the ASET 4 software. With the inputted conductivity, the potential difference values recorded by the SVET were automatically converted to current density values. For SVET tests, the probe (vibrating in planes perpendicular (Z) and parallel (X) to the surface of the sample) was placed at 100 ± 3 μm above the surface. The amplitude of vibration was 19 μm, and the vibrating frequencies of the probe were 174 Hz (X) and 73 Hz (Z). 35 × 25 points were obtained for each SVET map. Further details of the description of the experiment can be found in the work of Araujo et al. [11]. The samples from the SZ and BM were embedded, separately, in epoxy resin and used as the working electrode. The surface of the alloy was successively polished to a 1 μm surface finish. Adhesive tape and

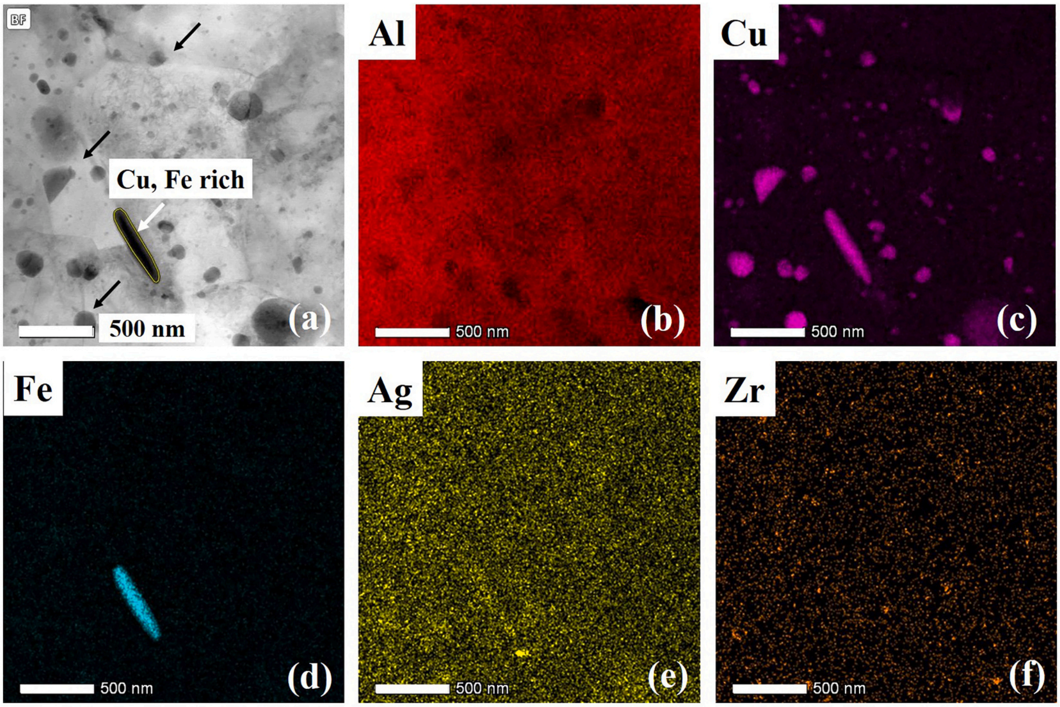

Fig. 3. (a) Bright-field image of the stir zone (SZ); (b-f) EDX maps showing the distribution of (b) Al, (c) Cu, (d) Fe, (e) Ag and (f) Zr. Black arrows indicate TB/T2 phase precipitates at grain boundaries.

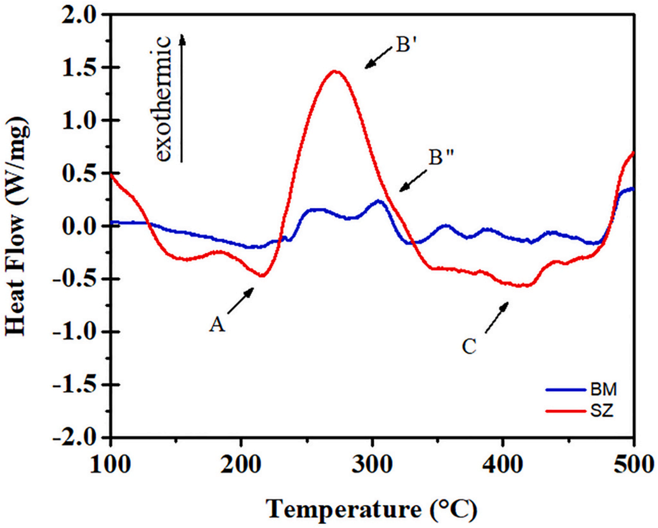

Fig. 4. DSC thermograms obtained at 10 °C/ min from the SZ and the BM of the AA2198-T8 alloy welded by FSW.

epoxy resin were used as the reservoir for the electrolyte in the SVET tests. Experiments were performed in a 0.005 mol L^{-1} NaCl solution for 24 h, and SVET maps were obtained every 2 h.

3. Results and discussion

3.1. Microstructural characterization

Fig. 1 (a) shows an optical macrograph of the AA2198-T8 alloy surface welded by friction stir welding (FSW), whilst Fig. 1 (b-e) show micrographs obtained from the surfaces of the base metal (BM) and stir zone (SZ). The differences in the grain morphologies of these zones can be easily seen. Fig. 1 (b) shows that the BM exhibit elongated grains in the direction of deformation, while in Fig. 1 (c) the SZ shows recrystallized grains, due to a combination of temperature and deformation caused by the FSW tool movement. Consequently, when compared the SZ and the BM microstructures, major variations are observed such as those in the distribution and size of constituent micrometric particles (Fig. 1 (d and e)). These particles are formed during alloy solidification and do not dissolve during thermomechanical processing [24]. However, the tool movement during welding process causes breakage of particles and their spread in the welding joint leading to a reduction in

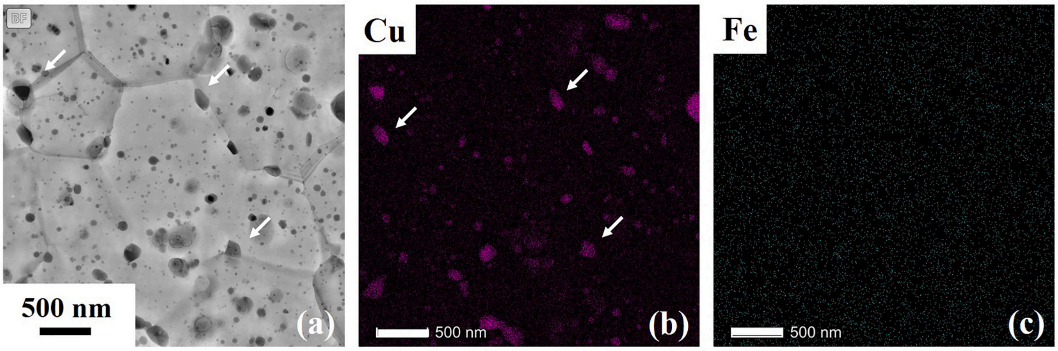

Fig. 5. (a) Bright-field images of the stir zone (SZ) showing the presence of Cu-enriched phases that have been identified as TB (Al_7Cu_4Li) and/or T2 (Al_6CuLi_3) phases. The arrows indicate some of these phases at grain boundaries; EDX maps showing the distribution of (b) Cu and (c) Fe in the area shown in (a).

size and particle distribution over the SZ [31,45]. Fig. 1 (d) shows the particles in the BM aligned according to the cold working direction, whereas in the SZ, Fig. 1 (e), they are distributed by the tool stir movement.

The constituent particles in both zones, BM and SZ, were mainly composed of Fe and Cu, Figs. 2 and 3, respectively. Besides, in the SZ (Fig. 3), a large number of Cu-rich precipitates, consisting of TB (Al_7Cu_4Li) / T2 (Al_6CuLi_3) phase, were found at the grain boundaries. These precipitates were not identified in the BM indicating that these were formed during FSW.

Besides the constituent particles, dispersoids mainly composed of Zr were also observed and were easily identified in the BM, Fig. 2 (f), but with reduced sizes and homogeneously distributed in the SZ, Fig. 3 (f). Zirconium is commonly added to Al alloys to promote the formation of dispersoids (Al_3Zr type) that control grain size by retarding recrystallization and grain growth [24,46]. These dispersoids are usually homogeneously dispersed in the matrix and have no direct effect on the alloy corrosion resistance [12]. Also, Ag-rich particles were found sparsely distributed in the BM of the alloy, Fig. 2 (e), but with lower sizes in the SZ, Fig. 3 (e). According to the literature [47,48], Ag addition reduces the solubility of Li in the Al matrix, promoting the nucleation of the T1 (Al_2CuLi) phase. Ag can also be found segregated at the matrix-precipitate interface.

The T1 phase is the main responsible for hardening in the third generation of Al-Cu-Li alloys [46]. Unlike the constituent particles, the primary strengthening precipitates, formed through ageing during T8 thermomechanical treatment, are widely affected by the heat produced during welding. This can lead to total or partial dissolution of these precipitates. Consequently, differences in the volume ratio of these precipitates across the weldment are expected. In the zones exposed to high temperatures, dissolution of the T1 phase, partial or total, occurs, leading to decreased hardness [33,34,49,50]. This was shown in previous work by comparison of the TEM images, temperature profile and microhardness of the AA2198-T8 alloy welded by FSW [7]. The T1 phase dissolution, either partial or total, resulted in the increasing softening from the BM (160 $HV_{0.2}$) to the SZ (120 $HV_{0.2}$), which was also confirmed by TEM analysis [7]. In the present work, the dissolution of T1 phase is supported by differencial scanning calorimetry results by a comparison of the thermograms of the BM and the SZ (Fig. 4). According to literature, the exothermic peak around 270 °C and its convolutions (peaks B′ and B″) are associated with the precipitation and coarsening of the T1 phase [23,51–53]. The area underneath a peak of DSC test is related to the precipitate volume fraction [51]. As observed in Fig. 4, the area under the peak B is smaller in the BM than in the SZ, revealing that the T1 phase in the SZ was present in lower content than in the BM, consequently, T1 precipitation occurred in larger amounts in the SZ compared to the BM where this phase was saturated. T1 phase dissolution occurs due to the high temperatures reached during FSW, and the elements Al, Cu and Li from T1 phase are solubilized in the matrix. Consequently, during the heating step of the DSC test, T1 phase in the SZ precipitates, explaining the high and large peak. Other differences between BM and SZ were seen; for instance at about 210 °C (peak A),

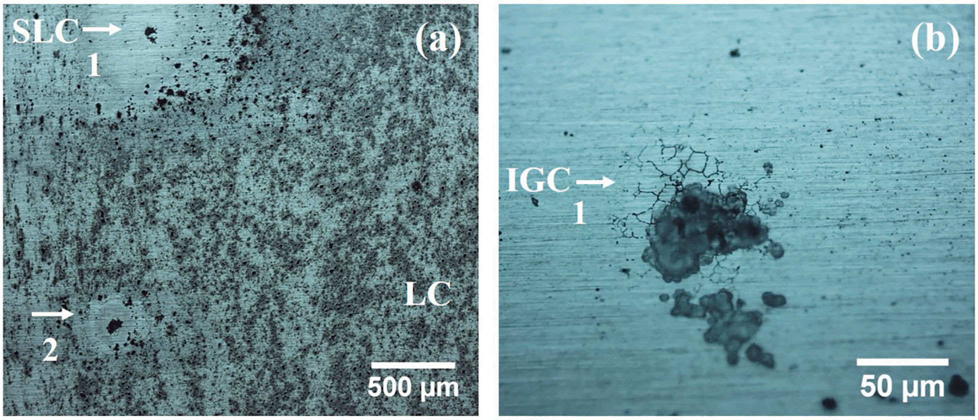

Fig. 6. (a) Surface of the stir zone (SZ) of the AA2198-T8 welded by friction stir welding (FSW) after 8 h of exposure in 0.005 mol L^{-1} NaCl solution; (b) higher magnification of the severe localized corrosion (SLC) indicated by “1” in (a) showing intergranular attack (IGC).

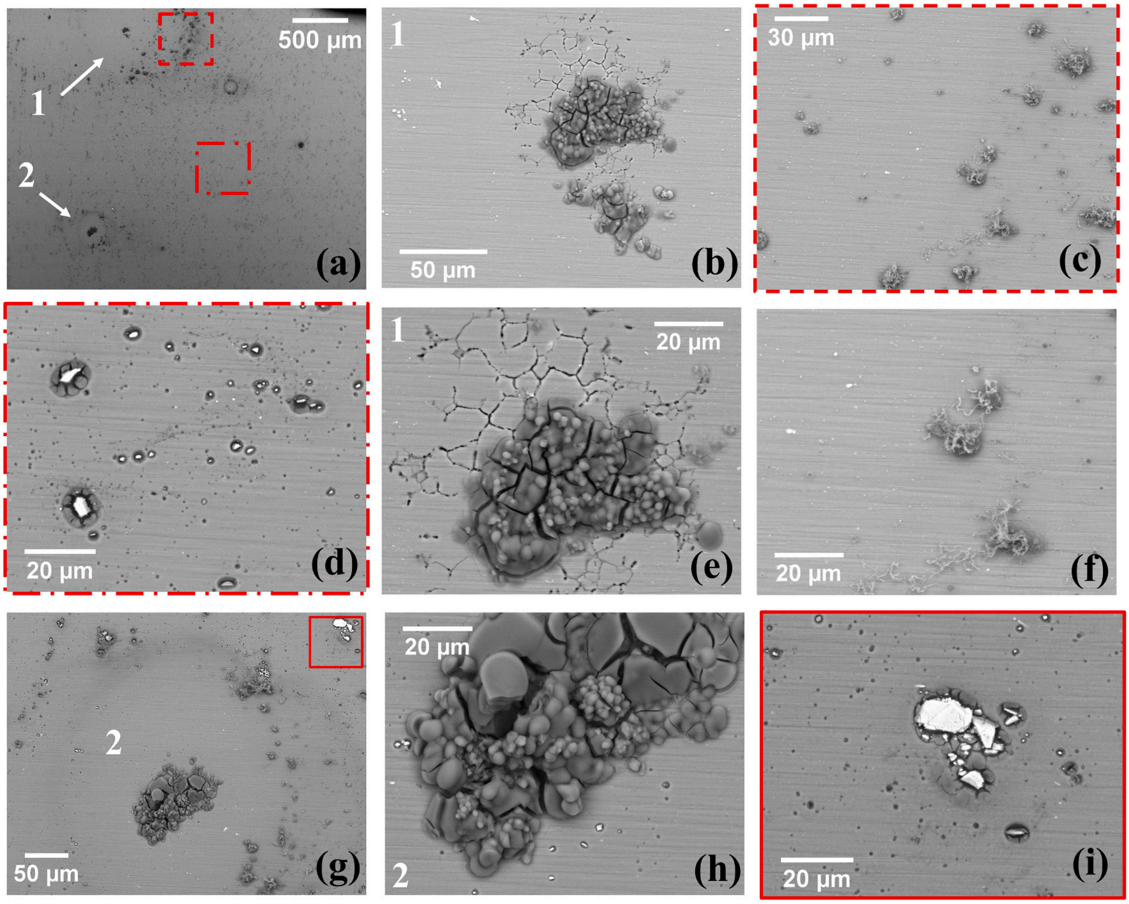

Fig. 7. SEM images of the surface of the stir zone (SZ) in the AA2198-T8 welded by friction stir welding (FSW) after 8 h of immersion in 0.005 mol L^{-1} NaCl showing (a) different corrosion morphologies; (b, e, g, h) severe localized corrosion (SLC); (c, f) corrosion products; and (d, i) localized corrosion (LC).

related to the dissolution of δ' (Al_3Li), and around 400 °C, the endothermic peak C associated with T1/TB dissolution in the SZ [23,45,51,54–57].

Rao et al. [40] investigated the nature of precipitates found in the SZ of the AA2198-T8 FSWed in order to understand the migration of Li after T1 phase dissolution. According to the authors, larger precipitates were found at grain boundaries, which were identified as T1 and TB phases, showing reprecipitation and coarsening of precipitates at these areas. In the present work, Fig. 3 shows several Cu-enriched precipitates detected in the SZ (indicated by black arrows), which were not seen in BM (Fig. 2). Since Fe was not identified in the composition of this precipitate, and Li cannot be detected by EDX, these precipitates in the SZ are most likely TB and/or T2 phases. This is supported by the literature that reports the formation of TB/T2 phases in the SZ of Al-Cu-Li alloys, due to T1 phase dissolution [8,39,40,45,54,56]. It is worth mentioning that, although T1, T2 and TB are composed of the same elements (Al, Cu and Li), they present different morphologies. The T1 phase shows needle-like morphology, whereas the T2 and TB phases have no regular geometric morphology [58], many of those being located at the grain boundaries, as indicated by black arrows in Fig. 3 (a).

Fig. 5 shows a micrograph of the SZ in which large amounts of T2/TB precipitates were found, highlighting the ones at grain boundaries (white arrows). Due to the amounts of Cu-rich precipitates along the grain boundaries, intergranular attack is expected in this zone due to galvanic coupling between the grain boundaries and the Al alloy matrix.

3.2. *Corrosion characterization*

3.2.1. *Stir zone (SZ)*

Intergranular corrosion (IGC) attack was in fact the main type of corrosion-related to localized corrosion sites, where severe localized corrosion (SLC) was identified after 8 h of exposure to the test solution (0.005 mol L^{-1} NaCl), as Fig. 6 shows.

In this condition, it is possible to differentiate the localized corrosion (LC), which is associated with the constituent particles and predominant over the surface, from the severe localized corrosion (SLC), and indicated by the arrows. Two SLC sites were identified on this surface (numbered as “1” and “2” in Fig. 6 (a)). The features of the SLC observed include protected zones around anodic sites and rings of corrosion products, delimiting the cathodic region. At higher magnification (Fig. 6b), the morphology of attack was observed revealing that the SLC in the SZ is related to intergranular attack.

Fig. 7 shows the details of the two SLC sites (identified as “1” and “2”) observed in Fig. 6. Site “2” was totally covered with corrosion products, whereas site “1” was only partially shielded. These observations reveal the singularity of each site and show that they can develop differently; pointing out that these features affect the electrochemical response.

Fig. 8 shows the corroded surface of another sample of the SZ, after 8 h of immersion in the 0.005 mol L^{-1} NaCl solution with the aim of showing the effects of the constituent particles (white particles) inside the protected zone surrounding the SLC pit. It can be seen that the particles and the matrix surrounding them were preserved, differently

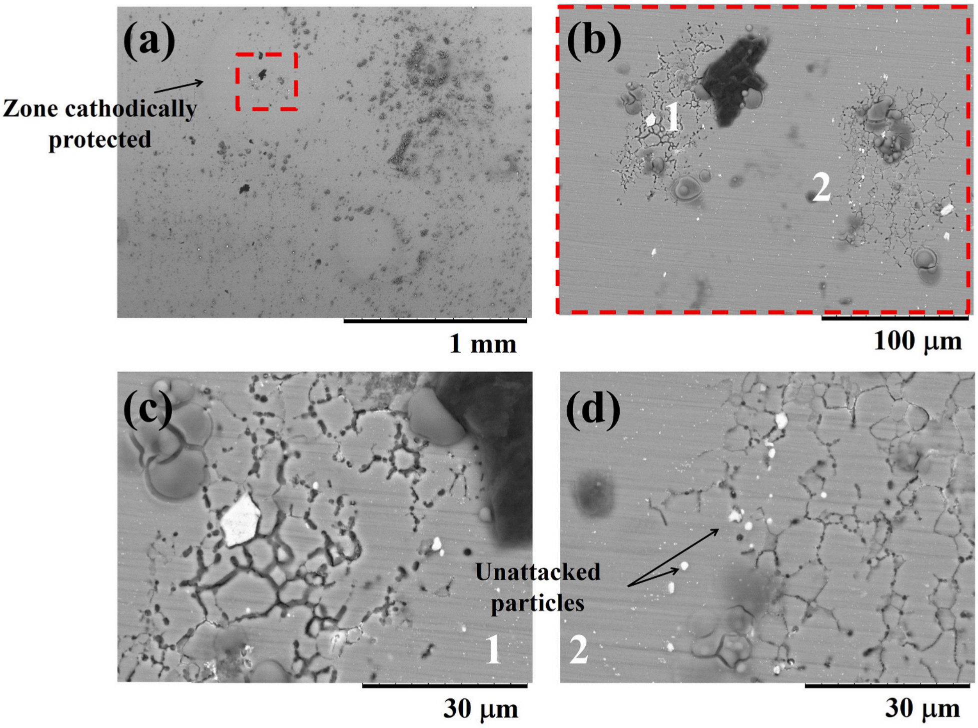

Fig. 8. (a) SEM image showing severe localized corrosion (SLC) in the stir zone (SZ) of the AA2198-T8 Al-Cu-Li alloy welded by friction stir welding (FSW) after 8 h of immersion in 0.005 mol L^{-1} NaCl solution; (b) higher magnification image of the squared region in (a); (c) higher magnification image of region “1” in (b); (d) higher magnification image of region “2” in (b).

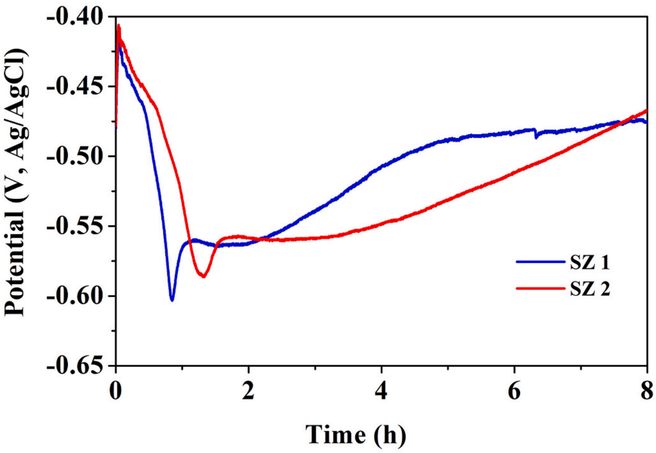

Fig. 9. Open circuit potential variation of the stir zone (SZ) samples during exposure to 0.005 mol L^{-1} NaCl solution.

from the same kind of particles located outside the cathodically protected region (Fig. 7 d, i). This result shows that the constituent particles did not interfere with the intergranular attack related to the SLC. No evidence of trenching around the remaining particles was observed (Fig. 8 c, d). This observation indicated that the T2/TB particles are the main reason for the intergranular attack associated with SLC.

It also can be seen in Fig. 8 that the precipitates at the grain boundaries were detached from the matrix. Comparing the morphology and size of the precipitates at the grain boundaries (Fig. 5) and the cavities originated by corrosion, it is possible to correlate the corrosion attack with the presence of the T2/TB phase. The corrosion mechanism related to the T2 phase is similar to that of T1 one [59,60]. Initially, the T2/TB precipitates are anodic relative to the matrix and these particles are activated and the anodic reaction is depolarized occurring the preferential dissolution of Al and Li in their composition leading to Cu enrichment in the particles. Consequently, the precipitate becomes cathodic to the matrix, leading to polarity reversal and anodic attack of the surrounding matrix with particles detachment from the surface. These observations are supported by the variation of the open circuit potential during 8 h of exposure of the sample in 0.005 mol L^{-1} NaCl

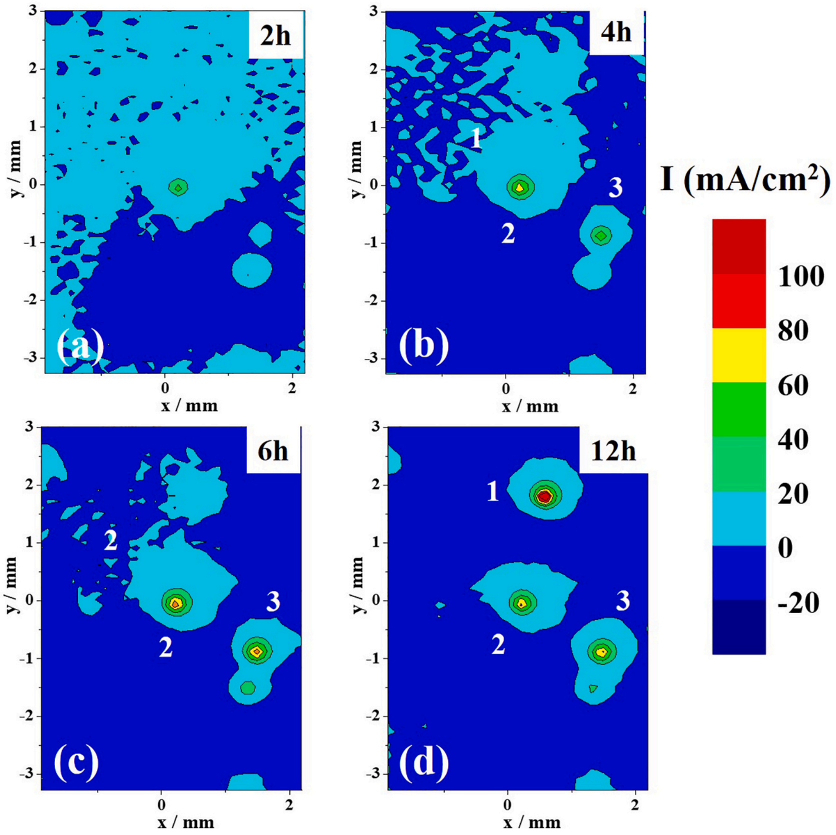

Fig. 10. (a-d) SVET maps obtained from the stir zone (SZ) of the AA2198-T8 Al-Cu-Li alloy welded by friction stir welding (FSW) after (a) 2 h; (b) 4 h; (c) 6 h and (d) 12 h of exposure to 0.005 mol L^{-1} NaCl solution.

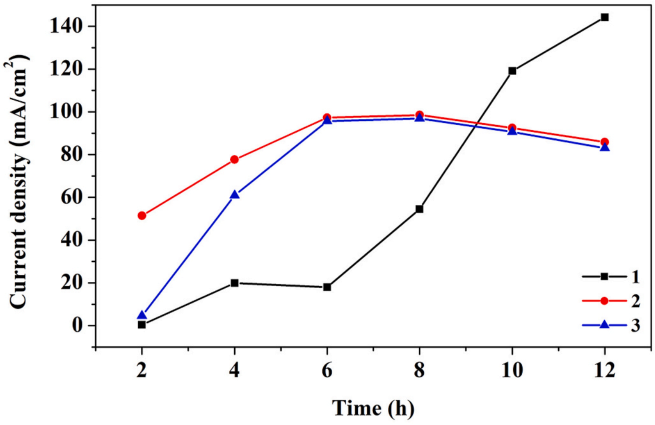

Fig. 11. Evolution of current density values with time of immersion in 0.005 mol L^{-1} NaCl solution for points 1, 2, and 3 of the stir zone (SZ) shown in Fig. 9 during scanning vibrating electrode technique (SVET) test.

solution, Fig. 8.

The potential drop seen below 2 h of immersion test in Fig. 9 is due to passive film breakdown followed by depolarization of the anodic reactions from increasing activation of the galvanic cells between the T2/TB phases and the matrix. As mentioned earlier, the galvanic micro-cells between T2/TB precipitates and the matrix lead to increasing attack of the adjacent matrix and posterior detachment of these precipitates, resulting in elimination of active sites. Subsequently, the passive film reforms at the sites from which particles are removed leading to consequent potential increase. The recovery of potential is not a fast process, and several complex effects may influence it, justifying the differences between the curves. First, it is influenced by the microstructure of the area analyzed and the quantities of T2/TB that are indeed involved in the corrosion process. Secondly, corrosion products formed on the anodic sites of the SLC (Fig. 7) could also be influencing the potential of the exposed surface, since it can hinder the corrosive

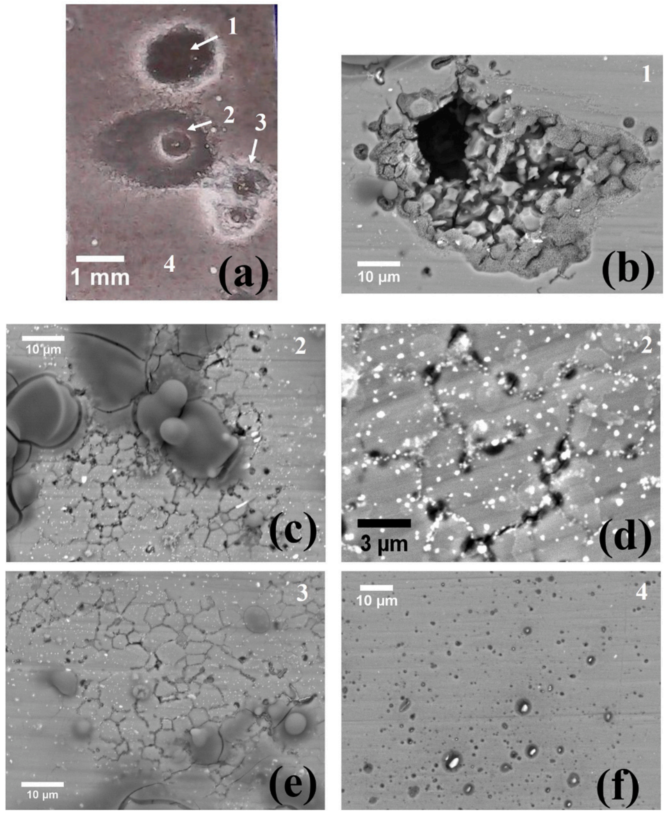

Fig. 12. (a) Optical and (b-f) SEM images of the stir zone (SZ) of the AA2198-T8 Al-Cu-Li alloy after 24 h of exposure in 0.005 mol L^{-1} NaCl solution for SVET analysis. (a) Optical image showing SLC sites. (b)-(c) SEM images of sites “1” and “2”, respectively. (d) Magnified image of the area shown in (c). (e)-(f) SEM images of sites “3” and “4”, respectively.

attack. In order to understand how these factors affect the potential, localized analyzes were performed.

The evolution of corrosion in the SZ was monitored by scanning vibrating electrode technique (SVET) during exposure in 0.005 mol L^{-1} NaCl solution for 12 h (Fig. 10). In the SVET maps, the development of SLC sites is indicated after 2 h of exposure and new sites continued to develop along the 12 h of test. Between 6 h and 12 h of test, the current densities related to sites 2 and 3 decreased, due to the accumulation of corrosion products or elimination of micro-cells, by the T2/TB phase removal. After 12 h of exposure, three SLC sites were identified. The current densities related to these sites were significantly higher than those associated with the constituent particles.

Fig. 11 compares the current densities of the three SLC sites indicated by “1”, “2” and “3” in Fig. 10 as a function of time of test. As indicated by the ionic current density maps (Fig. 10), the development of each region occurs independently, resulting in different behaviors. The electrochemical activity referring to positions “2” and “3” initially increases reaching a maximum current after 6 h of immersion. The current reduction observed after 6 h indicates decreased activity, likely associated with corrosion products deposition on these regions. On the other hand, the SLC related to “1” showed no reduction in electrochemical activity during 12 h of test and anodic current densities around 140 µA/cm^2 were reached after 12 h. This result suggests that in this site the conditions favored corrosion penetration/propagation and the pit mouth was not obstructed by corrosion products.

Fig. 12 (a) shows the surface of the SZ after 24 h of exposure in 0.005 mol L^{-1} NaCl solution for SVET map acquisition. As indicated by the anodic current values, the SLC site indicated as “1” (Fig. 12 (b)) apparently resulted in greater depth of penetration compared to sites “2” and “3”. Besides, unlike other sites (Fig. 12 (c, e)), SLC at site “1” did not show deposited corrosion products. Comparing the surface condition after the SVET test (Fig. 12), it is observed that all SLC regions were associated with intergranular corrosion. In addition, the localized attack related to the constituent particles that led to trenching was also observed outside the cathodically protected region (Fig. 12 (f)). It must be pointed out that due to the high current densities related to SLC, the resolution of current densities associated with the constituent particles by SVET was not possible.

The SVET results show that the anodic current densities were mainly concentrated at some sites and it became more evident with time of immersion (Fig. 10). This observation indicates that SLC sites provide the largest contribution to the global measurements, which helps to understand the profile observed during the OCP measurements (Fig. 9). As initially proposed, the initial drop is related to passive film breakdown and galvanic coupling between T2/TB phases and the matrix. This last phenomenon is reflected by the local increase in the current density (Fig. 11). As observed by the SVET maps, the current density is predominantly reduced over time, thus, the recovery of potential can be related to the decreased electrochemical activity on the majority of the exposed area, either by particles detachment or accumulation of corrosion products on the SLC sites.

3.2.2. *Base metal (BM)*

Fig. 13 shows the corrosion features in the BM after 8 h of exposure to the 0.005 mol L^{-1} NaCl solution. SLC was found and it was related to intragranular attack inside the area surrounding the pit mouth and also trenching was related to localized corrosion due to the constituent particles. Different from the features associated with the SLC in the SZ,

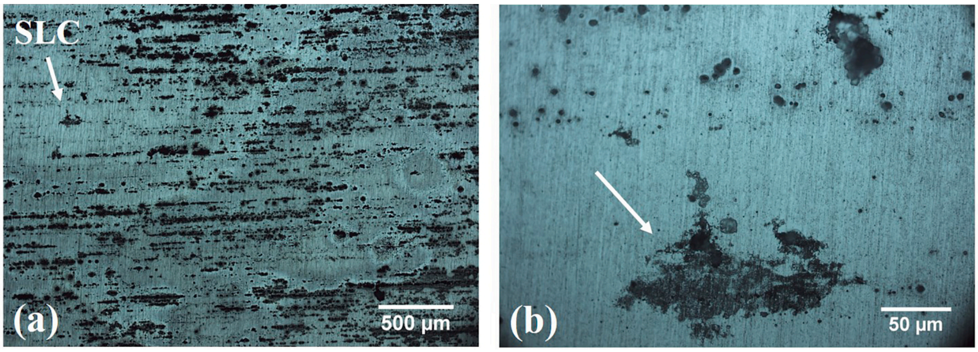

Fig. 13. (a) Optical micrography of the surface of the base metal (BM) of the AA2198-T8 Al-Cu-Li welded by friction stir welding (FSW) after 8 h of immersion in 0.005 mol L^{-1} NaCl solution; (b) higher magnification of the severe localized corrosion (SLC) indicated in (a).

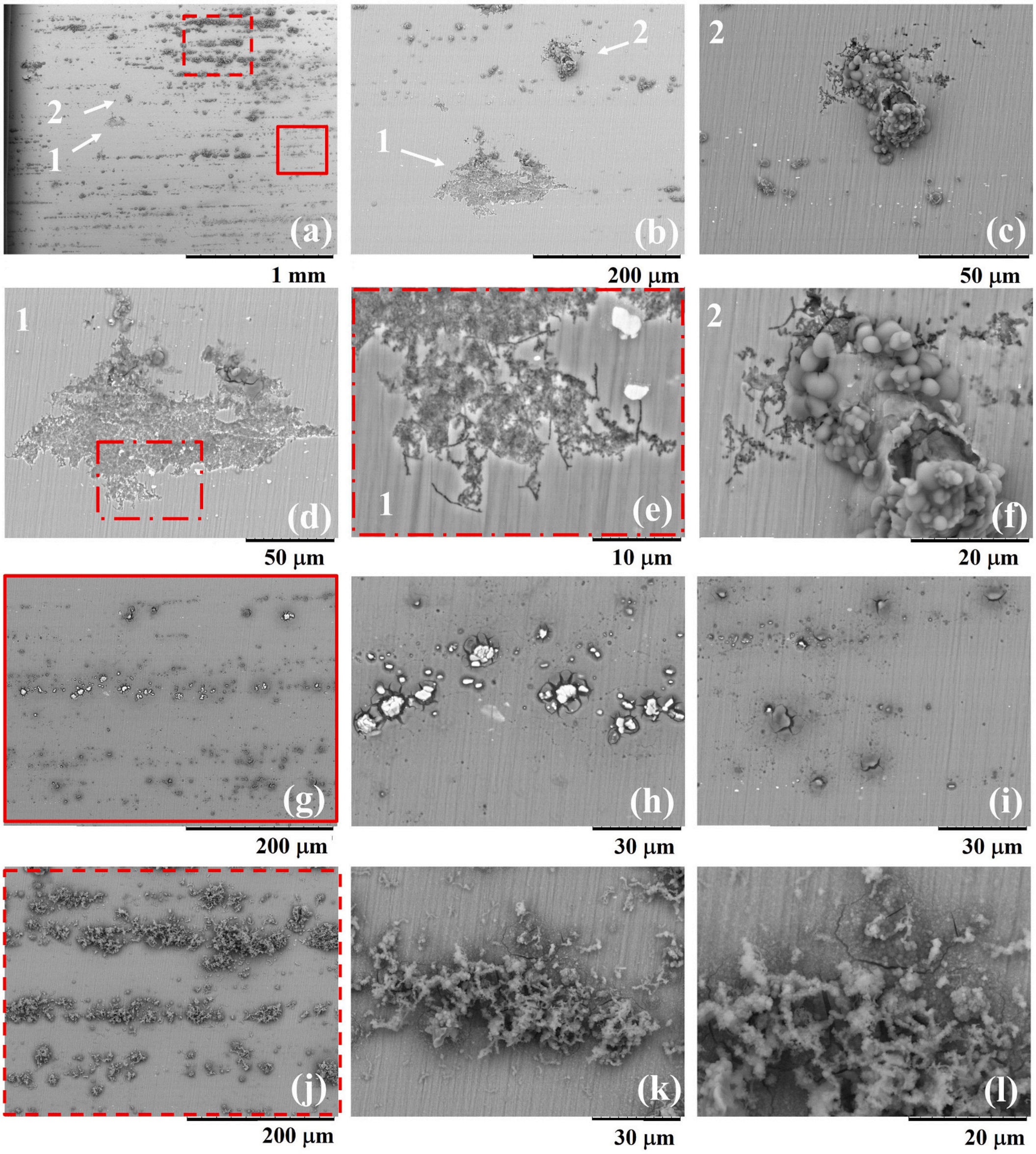

Fig. 14. (a) Surface of the base metal (BM) of the 2198-T8 Al-Cu-Li alloy welded by friction stir welding (FSW) after 8 h of immersion in 0.005 mol L^{-1} NaCl showing different types of corrosion morphologies; (b, d, e) higher magnification of severe localized corrosion (SLC) indicated by "1" in (a); (b, c, f) higher magnification of severe localized corrosion (SLC) indicated by "2" in (a); (g-i) localized corrosion associated with constituent particles; (j-l) corrosion products.

the area surrounding the SLC was not well defined due to the intragranular attack related to this type of attack and the elongated characteristics of the grains in this zone, and, consequently, the asymmetric current distribution.

Observation of the SLC in Fig. 13 at higher magnification (Fig. 14) shows the intragranular attack in the BM leading to the consumption of some grains and deposition of corrosion products at some sites (Fig. 14 b). The attack propagated through thin pathways inside the grains (Fig. 14 e), likely subgrain boundaries considering that the BM is not recrystallized. Besides the preferential precipitation of T1 phase at dislocations, this phase also favorably precipitates at subgrain boundaries. In a previous work [7] it was shown that T1 phase is abundant in the AA2198-T8 alloy, resulting in galvanic microcells between T1 phase and matrix and rapid corrosion propagation. The mechanism of corrosion attack related to T1 phase was previously mentioned and it is similar to that of the T2/TB phase, showing polarity reversal from anodic to cathodic due to selective Li dissolution and Cu- enrichment of the remaining phase [59].

Similar to the SZ, in the BM, the constituent particles located at the cathodically protected areas surrounding the mouths of the SLC pits remained preserved. The SLC site "2" (Fig. 14 e, f) presents similar features to the pathways observed in "1". However, the extension of the attacked areas was smaller in "2". Interestingly, sites "1" and "2" showed differences in corrosion products. It is proposed that site "2" corresponds to an early stage of SLC evolution when the amount of corrosion products generated is not sufficient to lead to their release from the surface. Fig. 14 (g-i) show trenching related to the micrometric particles outside the cathodically protected zone, while Fig. 14 (j-l) show corrosion products away from the SLC site. The similar behavior of constituent particles (Fig. 7 d and Fig. 14 h) in the SZ and BM confirms that these particles present the same behavior, cathodic to the matrix.

Fig. 15 shows the potential variations of the BM samples during 8 h

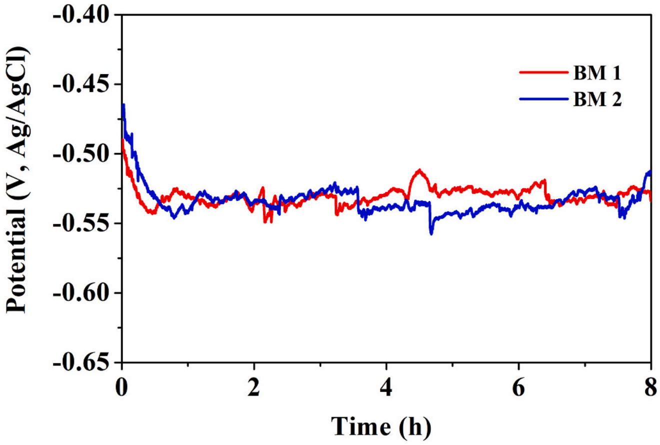

Fig. 15. Open circuit potential (OCP) variation with time of immersion in 0.005 mol L^{-1} NaCl solution for the base metal (BM) samples.

of exposure in 0.005 mol L^{-1} NaCl solution. The initial decrease in potential is due to passive film breakdown and depolarization of the anodic reactions in the test solution. However, potential increase does not occur in the BM and only potential oscillations along the test were observed, which is explained by the increased activation of new sites at the exposed surface followed by accumulation of deposited corrosion products on the active sites, as shown in Fig. 14 (j) – (l). These processes may occur simultaneously since the potential is kept approximately constant during the test, that is, the new SLC sites generated should provide a large current density to maintain the low potential even if other sites are obstructed.

The development of localized attack in the BM was also monitored by SVET during exposure to 0.005 mol L^{-1} NaCl solution (Fig. 16). After 2 h, two SLC sites (1 and 2) were identified and remained highly active up to 6 h. Between 6 and 12 h, the electrochemical activity measured at these two SLC sites decreased. At this period, electrochemical activity was detected at a new site (site 3). It is proposed that the decrease in current density related to sites “1” and “2”, between 6 and 12 h, was due to deposition of corrosion products at the mouths of the pit, hindering detection of the currents. At this same period, a new SLC area indicated as “3” was identified, as illustrated in the SVET map corresponding to 12 h of exposure.

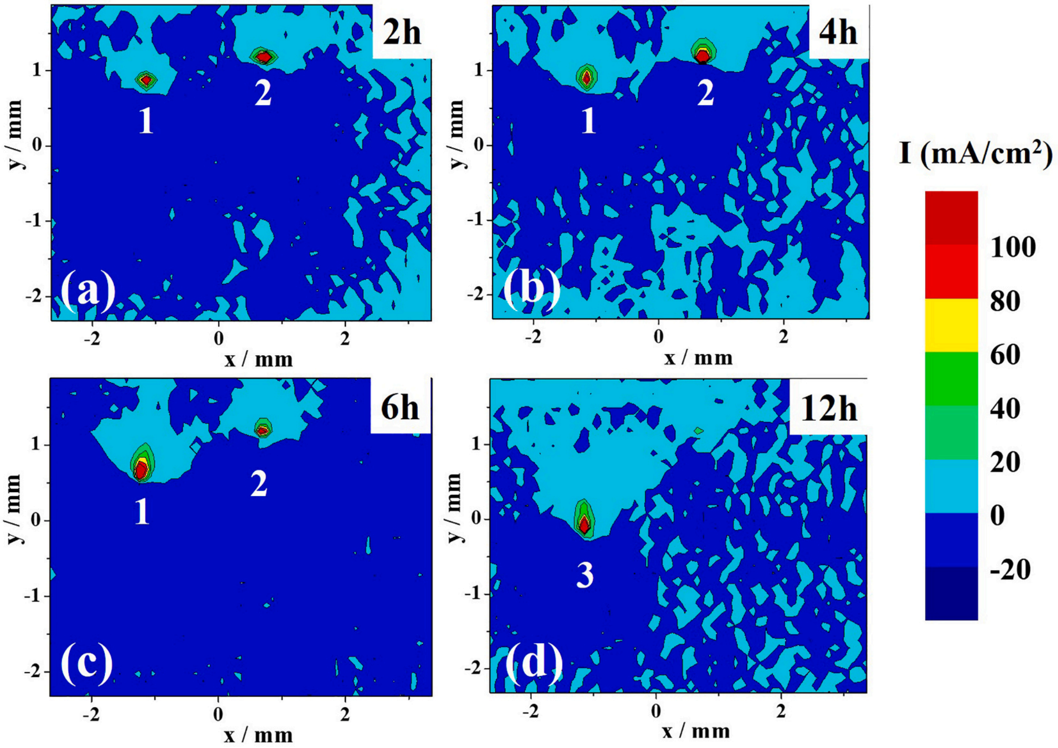

Fig. 16. Scanning vibrating electrode technique (SVET) maps of the base metal (BM) of AA2198-T8 obtained at (a) 2 h; (b) 4 h; (c) 6 h and (d) 12 h of exposure in 0.005 mol L^{-1} NaCl solution.

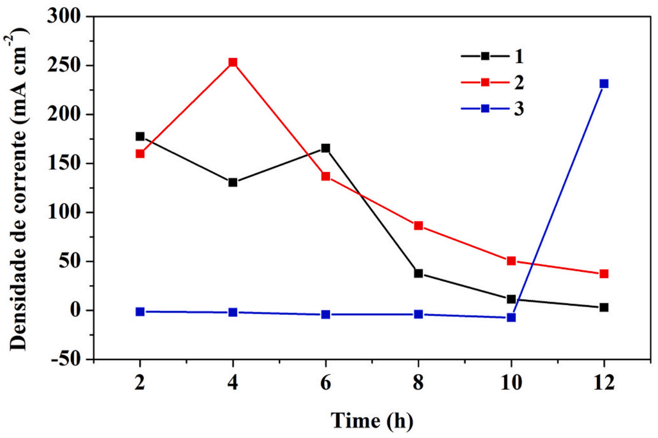

Fig. 17. Current density values obtained at points 1, 2, and 3 of the BM, shown in Fig. 16, as a function of time of exposure in 0.005 mol L^{-1} NaCl solution. Current density values were estimated from the SVET results.

Table 1
Comparison of the characteristics observed in the SZ and the BM.

	SZ	*BM*
Main microstructural characteristic related to SLC	T2/TB	T1
Localized current density at SLC sites (comparatively)	Max 140 μA/cm^2	Max 250 μA/cm^2

Fig. 17 displays the current density evolution as a function of time for the three SLC sites in Fig. 16. The maximum anodic current measured in the three sites varied in the range (170–250) μA/cm^2, that is, all above the maximum current density associated with the SLC related to the SZ, with values around 140 μA/cm^2. In addition, the period necessary to reach the maximum value of current can be very short, like 2 h, as observed by the behavior of site “3”. These results suggest that SLC is more severe in the BM than in the SZ. Moreover, the results support the premise of new sites being activated with time of exposure to the test solution, providing sufficient current density to keep almost constant the potential, despite some SLC sites in the BM were shielded by corrosion products.

3.2.3. *Stir zone versus base metal*

Although in literature [14,23,61] the SLC in Al-Cu-Li alloys has been commonly associated with the T1 phase, in this work, SLC was also observed in the SZ related to T2/TB phase. SVET results of the BM showed high current densities (above 150 μA/cm^2) only after 2 h of exposure to the test solution, a phenomenon related to the high electrochemical activity of the T1 phase, producing SLC associated to intragranular attack. On the other hand, in the SZ, SLC was related to intergranular attack due to T2/TB phase precipitated at grain boundaries. SVET measurements showed lower current densities for SLC in the SZ comparatively to the SLC at the BM. The current density values associated with the localized corrosion (LC) caused by the constituent particles Cu and Fe rich were significantly lower than those associated to the SLC and, consequently, were not resolved by SVET.

The electrochemical behavior of the SZ and BM showed significant differences, which could be easily identified by comparing the open circuit potential variation with time of the two tested zones. In the SZ, the variation of potential comprises drop followed by potential rise, with minimal oscillations, whereas in the BM the main drop was followed by continuous oscillations, with the potential being maintained at low values. These differences were explained by the distribution and characteristics of the nano-sized precipitates, summarized in Table 1. As mentioned previously, the current density provided by SLC associated with the T1 phase is superior to that of the attack related to T2/TB phases. Also, in both cases, SLC sites can be covered by corrosion products. However, to maintain the open circuit potential value measured after the main drop, the new SLC sites generated must provide sufficient current density to maintain the low potential values along the immersion test. Due to great amount of T1 phase inside grains of AA2198-T8 alloy [7,23,44], the micro-cells (T1 phase and matrix) can quickly connect each other facilitating the attack propagation that results in SLC [23] with high level of current density. Consequently, the potential in the BM is maintained at low values, even if corrosion products, due to the continuous activation of new electrochemical active areas, cover SLC sites. Thus, in the BM, oscillations are observed which are related to the competition between corrosion attack and deposition of corrosion products on the SLC sites hindering the access of the

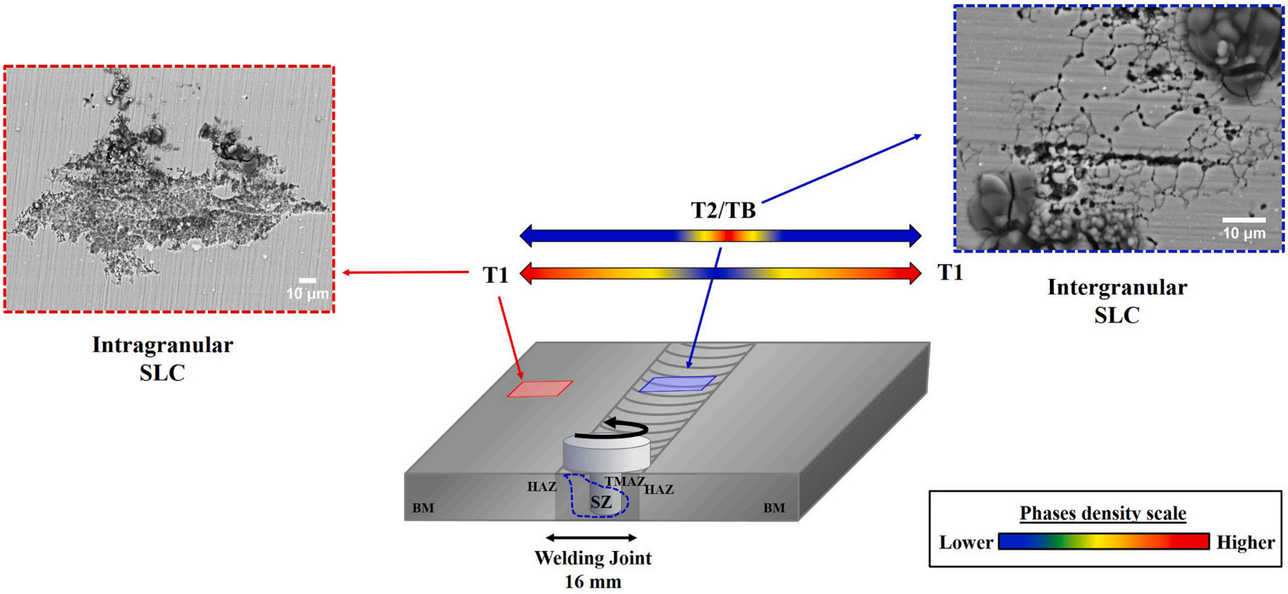

Fig. 18. Schematic diagram illustrating the differences between severe localized corrosion (SLC) observed in the base metal (BM) and the stir zone (SZ) of AA2198-T8 alloy welded by FSW.

corrosive medium to the Al alloy.

Fig. 18 presents a schematic diagram correlating precipitates, zones of welding and corrosion morphology of SLC.

4. Conclusions

The results of this study showed that the SZ of the AA2198-T8 Al-Cu-Li alloy welded by FSW present significant differences in its microstructure relatively to that of the BM with T1 phase dissolution and precipitation of T2/TB phase during FSW at the SZ. Electrochemical results showed also important differences in the maximum current densities related to the two zones, SZ and BM. Corrosion attack in the SZ was intergranular related to T2/TB phases preferentially precipitated at the grain boundaries. In the BM, corrosion attack was intragranular and related to T1 phase precipitated mainly at dislocations inside the grains. Localized corrosion (LC) resulting in trenching was related to the Cu- and Fe-enriched constituent particles and associated with lower current densities compared to SLC.

Data availability

The raw/processed data required to reproduce these findings cannot be shared at this time as the data also forms part of an ongoing study.

Declaration of Competing Interest

The authors declare that they have no known competing financial interests or personal relationships that could have appeared to influence the work reported in this paper.

Acknowledgements

The authors acknowledge to FAPESP (Proc. 2013/13235/6) and CAPES (Capes/Cofecub Proc. No806-14) for financial support for this work. The authors are thankful also to CAPES PROEX for the grants of Caruline de S. C. Machado (Grant no. 88882.333459/2019-01) and Mariana X. Milagre (Grant no. 88882.333479/2019-01) and FAPESP for the grants of Uyime Donatus (Proc.2017/03095-3) and João Victor de Sousa Araujo (Proc. 2019/18388-1). The authors are also thankful to Dr. Naga Vishnu Vardan Mogili from LnNANO for the TEM images and Dr. Nadine Pebere from INP for supply the material.

References

[1] P. Rambabu, N.E. Prasad, V.V. Kutumbarao, R.J.H. Wanhill, Aluminium alloys for aeroespace applications, in: Aerosp. Mater. Mater. Technol, Springer, 2017, pp. 29–72.
[2] T. Dursun, C. Soutis, Recent developments in advanced aircraft aluminium alloys, Mater. Des. 56 (2014) 862–871.
[3] P. Niskanen, T.H. Sanders, J.G. Rinker, M. Marek, Corrosion of aluminum alloys containing lithium, Corros. Sci. 22 (1982) 283–304.
[4] M. Pacchione, J. Telgkamp, Challenges of the metallic fuselage, in: 25Th Int. Congr. Aeronaut. Sci, 2006, pp. 1–12.
[5] S. Fei Zhang, W. Dong Zeng, W. Hua Yang, C. Ling Shi, H. Jun Wang, Ageing response of a Al-Cu-Li 2198 alloy, Mater. Des. 63 (2014) 368–374.
[6] M. Niedzinski, C. Thompson, Airware 2198 backbone of the falcon family of SpaceX launchers, Light Met. Age 68 (2010) 6–7.
[7] De C.S.C. Machado, U. Donatus, M.X. Milagre, N.V. Mogili, R.A.R. Giorjão, R. E. Klumpp, De J.V.S. Araujo, R.O. Ferreira, I. Costa, Correlating the modes of corrosion with microstructure in friction stir welded AA2198-T8 alloy in aqueous hydrogen peroxide-chloride medium, Corrosion 75 (2019) 628–640.
[8] U. Donatus, B.V.G. de Viveiros, M.C. de Alencar, R.O. Ferreira, M.X. Milagre, I. Costa, Correlation between corrosion resistance, anodic hydrogen evolution and microhardness in friction stir weldment of AA2198 alloy, Mater. Charact. 144 (2018) 99–112.
[9] J.A. Moreto, C.E.B. Marino, W.W. Bose Filho, L.A. Rocha, J.C.S. Fernandes, SVET, SKP and EIS study of the corrosion behaviour of high strength Al and Al-Li alloys used in aircraft fabrication, Corros. Sci. 84 (2014) 30–41.
[10] J.A. Moreto, E.E. Broday, L.S. Rossino, J.C.S. Fernandes, W.W. Bose Filho, Effect of localized corrosion on fatigue - crack growth in 2524-T3 and 2198-T851 aluminum alloys used as aircraft materials, J. Mater. Eng. Perform. 27 (2018) 1917–1926.
[11] De J.V.S. Araujo, U. Donatus, F.M. Queiroz, M. Terada, M.X. Milagre, M. Cavalieri, I. Costa, On the severe localized corrosion susceptibility of the AA2198-T851 alloy, Corros. Sci. 133 (2018) 132–140.
[12] U. Donatus, M. Terada, C. Ramirez, F. Martins, A. Fatima, S. Bugarin, I. Costa, On the AA2198-T851 alloy microstructure and its correlation with localized corrosion behaviour, Corros. Sci. 131 (2018) 300–309.
[13] Y. Zou, X. Chen, Corrosion behavior of 2198 Al – Cu – Li alloy in different aging stages in 3.5 wt % NaCl aqueous solution, J. Mater. Res. 33 (2018) 1–12.
[14] Y. Ma, X. Zhou, W. Huang, G.E. Thompson, X. Zhang, C. Luo, Z. Sun, Localized corrosion in AA2099-T83 aluminum-lithium alloy: the role of intermetallic particles, Mater. Chem. Phys. 161 (2015) 201–210.
[15] M. Guérin, J. Alexis, E. Andrieu, L. Laffont, W. Lefebvre, G. Odemer, C. Blanc, Identification of the metallurgical parameters explaining the corrosion susceptibility in a 2050 aluminium alloy, Corros. Sci. 102 (2016) 291–300.
[16] J.E. Kertz, P.I. Gouma, R.G. Buchheit, Localized corrosion susceptibility of Al-Li-Cu-Mg-Zn alloy AF/C458 due to interrupted quenching from solutionizing temperature, Metall. Mater. Trans. A 32 (2001) 2561–2573.
[17] X. Zhang, X. Zhou, T. Hashimoto, J. Lindsay, O. Ciuca, C. Luo, Z. Sun, X. Zhang, Z. Tang, The influence of grain structure on the corrosion behaviour of 2A97-T3 Al-Cu-Li alloy, Corros. Sci. 116 (2017) 14–21.
[18] X. Zhang, X. Zhou, Y. Ma, G.E. Thompson, C. Luo, Z. Sun, X. Zhang, Z. Tang, The propagation of localized corrosion in Al-Cu-Li alloy, Surf. Interface Anal. 48 (2016) 745–749.
[19] Y. Ma, X. Zhou, X. Meng, W. Huang, Y. Liao, Influence of thermomechanical treatments on localized corrosion susceptibility and propagation mechanism of AA2099 Al – Li alloy, Trans. Nonferrous Metals Soc. China 26 (2016) 1472–1481.
[20] J.F. Li, Z.Q. Zheng, N. Jiang, S.C. Li, Study on localized corrosion mechanism of 2195 Al-Li alloy in 4.0% NaCl solution (pH 6.5) using a three-electrode coupling system, Mater. Corros. 56 (2005) 192–196.
[21] M.X. Milagre, U. Donatus, C.S.C. Machado, De J.V.S. Araujo, R.M.P. Silva, B.V. G. De Viveiros, I. Costa, R. Maria, P. Silva, B.V.G. De Viveiros, A. Astarita, I. Costa, Comparison of the corrosion resistance of an Al – Cu alloy and an Al – Cu – Li alloy, Corros. Eng. Sci. Technol. (2019) 1–11.
[22] X. Lei, A. Saatchi, E. Ghanbari, R. Dang, W. Li, N. Wang, D.D. Macdonald, Studies on pitting corrosion of Al-Cu-Li alloys part I: effect of li addition by microstructural, electrochemical, in-situ, and pit depth analysis, Materials (Basel) 12 (2019) 19–22.
[23] De J.V.S. Araujo, De A.F. Santos, De C.S.C. Machado, F.M. Queiroz, M. Terada, A. Astarita, I. Costa, Thermomechanical treatment and corrosion resistance correlation in the AA2198 Al – Cu – Li alloy, Corros. Eng. Sci. Technol. (2019) 1–12.
[24] N. Birbilis, R.G. Buchheit, Electrochemical characteristics of intermetallic phases in aluminum alloys, J. Electrochem. Soc. 152 (2005) B140.
[25] A.E. Hughes, N. Birbilis, J.M.C. Mol, S.J. Garcia, X. Zhou, G.E. Thompson, High strength Al-alloys: Microstructure, corrosion and principles of protection, in: Z. Ahmad (Ed.), Recent Trends Process. Degrad. Alum. Alloy, Intech, Rijeka, 2011, pp. 223–262.
[26] W. Huang, Y. Ma, X. Zhou, X. Meng, Y. Liao, L. Chai, Y. Yi, X. Zhang, Correlation between localized plastic deformation and localized corrosion in AA2099 aluminum-lithium alloy, Surf. Interface Anal. 48 (2016) 838–842.
[27] X. Zhang, X. Zhou, T. Hashimoto, B. Liu, C. Luo, Z. Sun, Z. Tang, F. Lu, Y. Ma, Corrosion behaviour of 2A97-T6 Al-Cu-Li alloy: the influence of non-uniform precipitation, Corros. Sci. 132 (2018) 1–8.
[28] R. Yoshimura, T.J. Konno, E. Abe, K. Hiraga, Transmission electron microscopy study of the early stage of precipitates in aged Al-Li-cu alloys, Acta Mater. 51 (2003) 2891–2903.
[29] Y. Ma, X. Zhou, W. Huang, Y. Liao, X. Chen, X. Zhang, G.E. Thompson, Crystallographic defects induced localised corrosion in AA2099-T8 aluminium alloy, Corros. Eng. Sci. Technol. 50 (2015) 420–424.
[30] F. Campbell, Manufacturing Technology for Aerospace Structural Materials, Elsevier Science, 2006.
[31] R.S. Mishra, Z.Y. Ma, Friction stir welding and processing, Mater. Sci. Eng. R. Rep. 50 (2005) 1–78.
[32] P.L. Threadgill, A.J. Leonard, H.R. Shercliff, P.J. Withers, Friction stir welding of aluminium alloys, Int. Mater. Rev. 54 (2009) 49–93.
[33] P. Cavaliere, M. Cabibbo, F. Panella, A. Squillace, 2198 Al-Li plates joined by friction stir welding: mechanical and microstructural behavior, Mater. Des. 30 (2009) 3622–3631.
[34] M.X. Milagre, N.V. Mogili, U. Donatus, R.A.R. Giorjão, M. Terada, J.V.S. Araujo, C. S.C. Machado, I. Costa, On the microstructure characterization of the AA2098-T351 alloy welded by FSW, Mater. Charact. 140 (2018) 233–246.
[35] H. Long Qin, H. Zhang, D. Tong Sun, Q. Yu Zhuang, Corrosion behavior of the friction-stir-welded joints of 2A14-T6 aluminum alloy, Int. J. Miner. Metall. Mater. 22 (2015) 627–638.
[36] V. Proton, J. Alexis, E. Andrieu, C. Blanc, J. Delfosse, L. Lacroix, G. Odemer, Influence of post-welding heat treatment on the corrosion behavior of a 2050-T3 aluminum-copper-lithium alloy friction stir welding joint, J. Electrochem. Soc. 158 (2011) C139.
[37] M. Dhondt, I. Aubert, N. Saintier, J.-M. Olive, Intergranular stress corrosion cracking of friction stir welded nugget on a 2050-T8 aluminum alloy, Adv. Mater. Sci. 11 (2011) 43–50.
[38] V. Proton, J. Alexis, E. Andrieu, J. Delfosse, M.C. Lafont, C. Blanc, Characterisation and understanding of the corrosion behaviour of the nugget in a 2050 aluminium alloy friction stir welding joint, Corros. Sci. 73 (2013) 130–142.
[39] J.A. Schneider, A.C. Jr Nunes, P.S. Chen, G. Steele, TEM study of the FSW nugget in AA2195-T81, J. Mater. Sci. 40 (2005) 4341–4345.

[40] J. Rao, E.J. Payton, C. Somsen, K. Neuking, G. Eggeler, A. Kostka, J.F. Santos, Where does the lithium go ? – a study of the precipitates in the stir zone of a friction stir weld in a Li-containing 2xxx series Al alloy, Adv. Eng. Mater. (2010) 298–303.

[41] X. Zhang, B. Liu, X. Zhou, J. Wang, C. Luo, Z. Sun, Z. Tang, F. Lu, Corrosion behavior of friction stir welded 2A97 Al-Cu-Li alloy, Corrosion 73 (2017) 988–997.

[42] M.X. Milagre, U. Donatus, C.S.C. Machado, J.V.S. Araujo, R.O. Ferreira, R.M. P. Silva, R.A. Antunes, I. Costa, Exfoliation corrosion susceptibility in the zones of friction stir welded AA2098-T351, J. Mater. Res. Technol. 8 (2019) 5916–5929.

[43] N. Jadhav, V.J. Gelling, Review—the use of localized electrochemical techniques for corrosion studies, J. Electrochem. Soc. 166 (2019) 3461–3476.

[44] J.V.S. Araujo, R.M.P. da Silva, U. Donatus, De C.S.C. Machado, I. Costa, Microstructural, electrochemical and localized corrosion characterization of the AA2198-T851 Alloy, Mater. Res. 23 (2020) 1–10.

[45] U. Donatus, R.M.P. da Silva, De J.V.S. Araujo, M.X. Milagre, De C.P. Abreu, De C.S. C. Machado, I. Costa, Macro and microgalvanic interactions in friction stir weldment of AA2198-T851 alloy, J. Mater. Res. Technol. 8 (2019) 6209–6222.

[46] N.E. Prasad, T.R. Ramachandran, Phase Diagrams and Phase Reactions in Al-Li Alloys, Elsevier Inc., 2013.

[47] R.S. Mishra, H. Sidhar, Physical metallurgy of 2XXX aluminum alloys, in: Frict. Stir Weld. 2XXX Alum. Alloy. Incl. Al-Li Alloy, Butterworth-Heinemann, Oxford, 2017, pp. 15–36.

[48] A. Cho, R.E. Greene, M.H. Skillingberg, P.S. Fielding, Aluminum-lithium alloys for aerospace applications workshop: Proceedings of a workshop held at NASA, in: B. N. Bhat, T.T. Bales, E.J. Vesely (Eds.), Al-Li Alloy Dev. Reynolds Met. Co. Aerosp. Appl, Marshall Space Flight Center, Alabama, 1994, pp. 17–22.

[49] T. Le Jolu, T.F. Morgeneyer, A.F. Gourgues-Lorenzon, Effect of joint line remnant on fatigue lifetime of friction stir welded Al–Cu–Li alloy, Sci. Technol. Weld. Join. 15 (2010) 694–698.

[50] H. Sidhar, R.S. Mishra, Aging kinetics of friction stir welded Al-Cu-Li-Mg-Ag and Al-Cu-Li-Mg alloys, Mater. Des. 110 (2016) 60–71.

[51] H. Qin, H. Zhang, H. Wu, The evolution of precipitation and microstructure in friction stir welded 2195-T8 Al-Li alloy, Mater. Sci. Eng. A 626 (2015) 322–329.

[52] S. Ahmadi, A. Shokuhfar, M.R. Abotalebi, A. Rezaei, A calorimetric study on the precipitation of T1 phase during the ageing of an Al-Li-Cu-Zr alloy, Defect Diffus. Forum. 273–276 (2008) 14–17.

[53] M.X. Milagre, N.V. Mogili, U. Donatus, R.A.R. Giorjão, M. Terada, J.V.S. Araujo, C. S.C. Machado, I. Costa, On the microstructure characterization of the AA2098-T351 alloy welded by FSW, Mater. Charact. 140 (2018) 233–246.

[54] A. Steuwer, M. Dumont, J. Altenkirch, S. Birosca, A. Deschamps, P.B. Prangnell, P. J. Withers, A combined approach to microstructure mapping of an Al-Li AA2199 friction stir weld, Acta Mater. 59 (2011) 3002–3011.

[55] M.J. Starink, P. Wang, I. Sinclair, P.J. Gregson, Microstructure and strengthening of Al-Li-Cu-Mg alloys and MMCS: i. Analysis and modelling of microstructural changes, Acta Mater. 47 (1999) 3841–3853.

[56] J. Entringer, M. Reimann, A. Norman, J.F. Dos Santos, Influence of Cu/Li ratio on the microstructure evolution of bobbin-tool friction stir welded Al-Cu-Li alloys, J. Mater. Res. Technol. 8 (2019) 2031–2040.

[57] N. Gao, M.J. Starink, L. Davin, A. Cerezo, S.C. Wang, P.J. Gregson, Microstructure and precipitation in Al-Li-Cu-Mg-(Mn, Zr) alloys, Mater. Sci. Technol. 21 (2005) 1010–1018.

[58] T. Dorin, A. Vahid, J. Lamb, Aluminium lithium alloys, in: Fundam. Alum. Metall, Elsevier Ltd., 2018, pp. 387–438, https://doi.org/10.1016/B978-0-08-102063-0.00011-4.

[59] J.F. Li, Z.Q. Zheng, S.C. Li, W.J. Chen, W.D. Ren, X.S. Zhao, Simulation study on function mechanism of some precipitates in localized corrosion of Al alloys, Corros. Sci. 49 (2007) 2436–2449.

[60] J.F. Li, C.X. Li, Z.W. Peng, W.J. Chen, Z.Q. Zheng, Corrosion mechanism associated with T1 and T2 precipitates of Al-cu-Li alloys in NaCl solution, J. Alloys Compd. 460 (2008) 688–693.

[61] Y. Ma, X. Zhou, Y. Liao, Y. Yi, H. Wu, Z. Wang, W. Huang, Localised corrosion in AA 2099-T83 aluminium-lithium alloy: the role of grain orientation, Corros. Sci. 107 (2016) 41–48.